Ultrastructural characterization of a viral RNA and G-protein containing, membranous organelle formed in respiratory syncytial virus infected cells

Swetha Vijayakrishnan[1], Andrew M Burns[1], Emmeline L Blanchard[2], Matthew C Spink[3], James Gilchrist[3], Andrew Howe[3], Michelle C Darrow[3,4], Maria Harkiolaki[3], Cheng-Yu Wu[5], Rebecca Ellis Dutch[5], Philip J. Santangelo[2], Rachel Fearns[6*], David Bhella[1*]

Abstract

Respiratory syncytial virus (RSV) is a leading cause of respiratory disease in infants and the elderly. In common with most viruses that replicate in the host cell cytoplasm, RSV induces the formation of cytoplasmic compartments within infected cells to sequester replicative processes from host countermeasures. The best characterised organelle formed during RSV infection is the inclusion body – the primary site of viral RNA synthesis - thought to form as a membrane-less biomolecular condensate. Fluorescence microscopy of cellular compartments using probes directed at the structural proteins of RSV and the intergenic regions of the RSV genome have identified a second class of organelles termed assembly granules. Here we use correlative microscopy to identify assembly granules in the cytoplasm of frozen hydrated RSV infected cells for imaging using cryogenic soft X-ray tomography and cryogenic electron tomography. We show that these compartments are membrane bound, enclosing large numbers of vesicles, some of which contain RSV ribonucleoprotein complexes. Further we show that these organelles are frequently adjacent to mitochondria and surrounded by ER-like membranes. We also observe vesicles connected by junctions suggesting mixing of contents and a mechanism for the different viral proteins to come together within the assembly granule prior to budding. Collectively, our data provides novel insights into the RSV assembly process.

Introduction

Respiratory syncytial virus (RSV) is a major cause of respiratory disease, causing bronchiolitis in infants and acute respiratory failure in the elderly. It is estimated to cause more than 30M infections globally each year in children under the age of five, resulting in ~3M hospital admissions and 60,000 in-hospital deaths [1]. In older adults an estimated ~330,000 hospital admissions lead to 14,000 in-hospital deaths globally each year [2].

RSV is an enveloped virus, classified within the *Orthopneumovirus* genus of the Mononegavirales, a group of non-segmented, negative sense RNA containing viruses [3]. The viral genome is 15.2 kb and encodes

[1] MRC-University of Glasgow Centre for Virus Research, Garscube campus, 464 Bearsden Road, Glasgow, UK

[2] Wallace H. Coulter Department of Biomedical Engineering, Georgia Institute of Technology and Emory University, Atlanta, Georgia, USA

[3] Diamond Light source, Harwell Science and Innovation campus, Didcot, UK

[4] Rosalind Franklin Institute, Harwell Science & Innovation Campus, Didcot, UK

[5] Department of Molecular and Cellular Biochemistry, University of Kentucky, Lexington, Kentucky, USA

[6] Department of Microbiology and National Emerging Infectious Diseases, Laboratories, Boston University Chobanian & Avedisian School of Medicine, Boston, Massachusetts, USA

* Corresponding authors - Email : David.Bhella@glasgow.ac.uk, rfearns@bu.edu

eleven gene products in ten open reading frames [4, 5]. Throughout the viral replication cycle, the genome is encapsidated along its length by multiple copies of nucleocapsid protein (N) forming a helical ribonucleoprotein complex, known as the nucleocapsid. Nucleocapsids associate with proteins involved in viral transcription and genome replication; the large RNA-dependent RNA-polymerase subunit (L); phosphoprotein (P); and M2-1 protein, forming holonucleocapsids.

RSV assembles filamentous virions that contain multiple holonucleocapsids, as well as N-RNA rings. These are surrounded by a layer of helically ordered matrix (M) protein that is in turn enclosed within the viral envelope studded by viral glycoproteins F, G and SH [6]. Following G mediated attachment of a virion to a new host-cell, F drives fusion of the viral envelope with the plasma membrane [7, 8], leading to release of holonucleocapsids into the cell cytoplasm, where they commence synthesis of viral RNA: mRNAs corresponding to each of the viral genes, and antigenomes that in turn act as templates for the synthesis of new genome copies [5]. Viral replication takes place exclusively in the cytoplasm of the host cell. Accumulation of virus-encoded proteins and genome copies leads to the production of progeny filamentous virions that bud from the plasma membrane [9].

In previous work, fluorescence microscopy studies characterised the relationships between RSV RNA and proteins, defining their location within infected cells at different times of infection. At early times, the RSV genomic RNA and L, P, N and M2-1 proteins co-localised in small puncta [10]. As the infection progresses the puncta increase in size to form a second type of compartment: large inclusion bodies, which have been shown to be sites of RSV RNA synthesis [10, 11]. The inclusion bodies are membrane-less structures that have properties of liquid-liquid phase-separated organelles [12]. Anecdotal evidence suggests that they are densely packed. For example, while inclusion body-associated RSV genome RNA has been detected with standard fluorescence *in situ* hybridization (FISH) probes, it was not readily detected using chemically modified RNA probes targeting the RSV genome, known as MTRIPs (multiply labelled tetravalent RNA imaging probes). In addition, immunofluorescence labelling of N and P proteins primarily detected them at the inclusion body surface, likely indicating epitope occlusion in the inclusion body interior [11]. Later times in infection mark the appearance of a third type of compartment containing RSV ribonucleoprotein structures [10]. These cytoplasmic granules also contain the viral M protein, the attachment (G) and fusion (F) glycoproteins and are thought to be important in bringing together viral components required for virion assembly. Based on these observations they have been tentatively termed assembly granules [10, 13]. Assembly granules appear to have different biophysical properties than inclusion bodies: whereas inclusion bodies seem to be dense and partially impenetrable, assembly granules are permeable to MTRIP probes, and N and P proteins can be readily detected throughout, rather than predominantly at the periphery [13]. While considerable work has been performed to characterise RSV inclusion bodies, little is known regarding the properties of assembly granules.

Detailed characterisation of the diverse cellular compartments formed during RSV infection is a key step towards mechanistic properties being properly ascribed to well-defined organelles. To begin to address this challenge, we used correlative fluorescence microscopy under cryogenic conditions to identify compartments of interest for imaging using both soft X-ray tomography (cryo-SXT), and electron tomography (cryo-ET). These techniques provide a means of imaging cells in a near-native, frozen-hydrated state, without chemical fixation that may cause artefacts or perturbation of important features. Cryo-SXT provides high contrast imaging of intact cells, to reveal cellular ultrastructure by operating in the ‘water-window’ of X-ray light. This is the spectral range between the absorbance edge of carbon (284 eV) and that of oxygen (543 eV). Thus, images generated by X-rays at an energy of ~500 eV give much greater absorbance contrast for carbon and nitrogen containing materials such as protein and lipids, compared to oxygen containing water [14, 15]. Cryo-SXT gives a wide field of view (potentially many tens of μm) with resolution ranging between 25 and 40 nm depending on the optical system used. Cryo-SXT is therefore particularly suited to imaging membranous cellular compartments. Cryo-ET provides complementary three-dimensional imaging of unfixed frozen-hydrated cellular samples, providing a higher resolution view (typically in the 1-2 nm range), but over a smaller field of view of ~1-2 μm. The limited penetrating power of electrons in the transmission electron microscope restricts sample thickness to <300 nm. To overcome this limitation, cellular specimens may be milled using a focused ion beam, to produce lamellae of appropriate thickness (cryoFIB milling) [16].

We used multi-modal cryomicroscopy imaging to investigate the structure of cellular compartments formed during RSV infection, focusing on assembly granules, which were detected using RSV genome targeted MTRIPs and G-specific lectin probes. The images obtained revealed that assembly granules are multivesicular compartments that contain both nucleocapsids and N-RNA rings and demonstrate evidence of vesicle-vesicle fusion events that could allow different viral components to be brought together.

Results

RSV MTRIP-labelled compartments are distinct from canonical inclusion bodies

RSV MTRIP probes (RSV MTRIPs), which target an intergenic region of the negative sense genome RNA, are particularly suited to live-cell imaging, making them ideal probes for cryomicroscopy without chemical fixation. To characterize the different organelles detected by RSV MTRIPs, RSV protein co-localisation studies were performed using laser-scanning confocal microscopy on cells that had been fixed at 24 h post infection (pi). Bright cytoplasmic puncta were observed with MTRIP staining, which was specific to RSV-infected cells (Figs 1A & 1B, supplementary Fig S1). Co-localisation analyses indicated a complex array of RSV-infection associated cellular compartments. Co-staining with MTRIPs and N-specific antibody revealed at least three types of cytoplasmic compartments. MTRIP and N co-localization was observed but confined to small compartments at the cell periphery (Figs 1C & 1D) and inside budding filamentous virions (Figs 1E-1H). In addition to these N and RSV genome containing compartments, many small granules were positive only for MTRIP-labelling (Fig. 1K & 1L). This is a surprising finding because it is thought that RSV genome RNA only exists in encapsidated form. It is possible that in these compartments, RNA-bound N protein adopts a conformation that occludes the antibody epitope, or that they contain viral genome RNA (or a fragment of genome RNA) that is not encapsidated. In addition to these relatively small compartments, N-specific staining was present in larger compartments, with strong staining at the periphery, but weaker staining at the centre. These larger structures, which exhibit the established staining characteristics of canonical RSV inclusion bodies were devoid of any MTRIP labelling (Figs 1I & 1J) corroborating previous observations [11, 17]. MTRIP co-staining experiments with an RSV P-targeted fluorescent antibody confirmed that P was

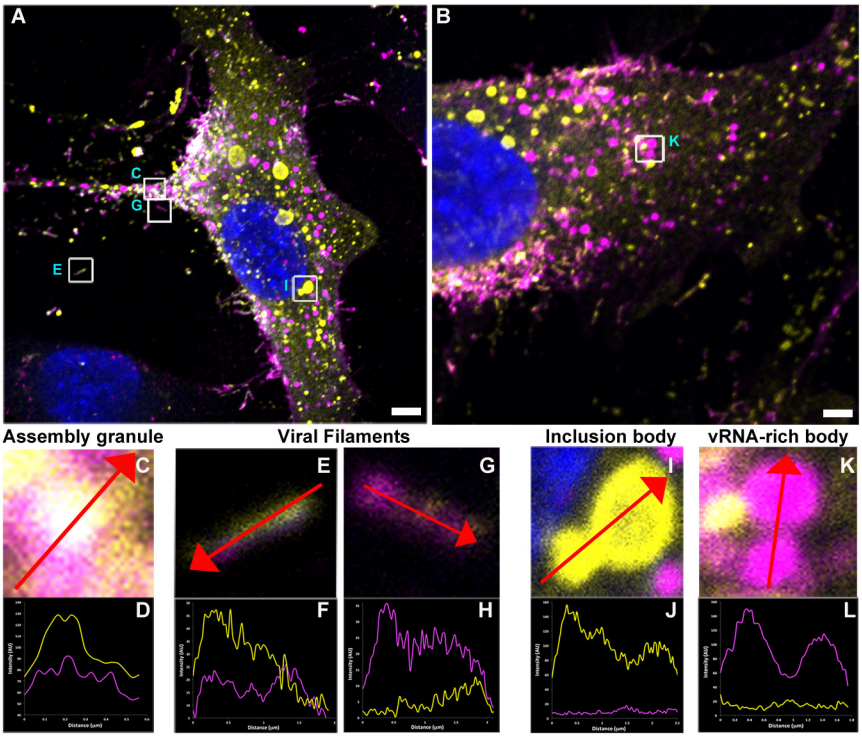

Figure 1. Viral RNA and RSV N co-localise in small cytoplasmic compartments. (A and B) A549 cells were infected with RSV at an MOI of 3, labelled with MTRIPs and subsequently fixed at 24h pi. Cells were stained for N (yellow), viral RNA MTRIP staining is shown in pink, nuclei were stained with DAPI (blue). Representative merged channel images of a single plane are shown. The scale bar represents 5 µm. Enlarged views of regions indicated by white rectangles. Letters labelled in cyan adjacent to the white rectangles correspond to the insets in the panel below highlighting cytoplasmic structures observed upon RSV infection. **(C and D)** show co-localisation of MTRIP and N antibody staining in small compartments within the cytoplasm. Co-localisation is also seen in viral filaments at the cell surface **(E to H)**. **(I and J)** Large compartments reminiscent of those previously described as inclusion bodies show staining by anti-N but no MTRIP labelling of viral RNA, **(K and L)** while small granular viral RNA-rich bodies are seen in abundance. Intensity plots are drawn along the red lines of the enlarged images.

largely detected in inclusion bodies, showing a similar pattern of staining to that of N (supplementary Figs S2A-S2G). Like N however, co-localisation of P and MTRIP staining of RSV RNA was observed in some small granular structures as well as RSV filamentous virions along the cell periphery (supplementary Figs S2H-S2K).

Viral glycoproteins F and G play a key role in RSV infection. F is required for virion fusion with the cell membrane and subsequent entry into cells, while G mediates virion attachment. Both G and F could be found co-localised with MTRIPs, in small cytosolic compartments (Fig 2, S3).

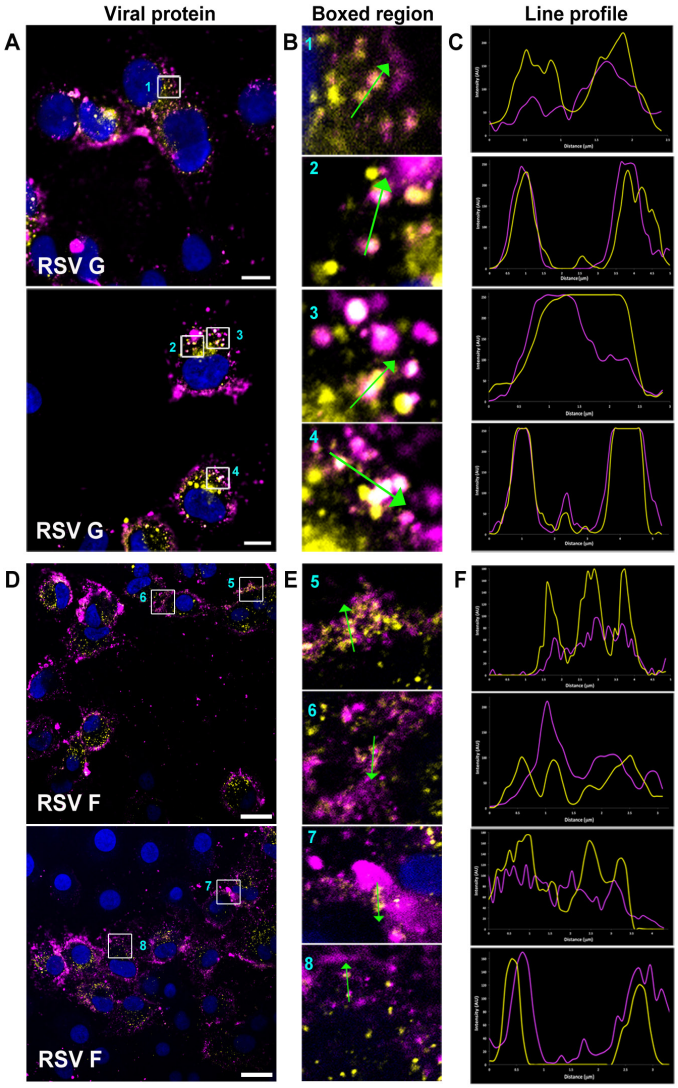

Figure 2. RSV G and F co-localise with viral RNA. A549 cells infected with RSV at an MOI of 3 were labelled with MTRIPs at 24h pi and subsequently fixed and stained for RSV glycoproteins **(A)** G and **(D)** F. Scale bar is 10 µm in (A) and 20 µm in (D). Staining for nucleus (blue), G or F (yellow) and MTRIPs (pink) are shown. Representtive images of a single plane are shown. Enlarged cropped images (white squares) are numerically labelled (cyan) and correspond to the insets shown in panels B and E**. (B-C, E-F)** Enlarged boxed images from (A and D) indicated by white squares show the distribution and co-localisation of staining in punctate structures. **(B)** RSV G and MTRIPs co-localise throughout the cytosol while **(E)** RSV F and MTRIPs seem to co-localise largely at the edge of the cell. Line profiles showed a higher degree of co-localisation for viral RNA with G **(C)** than with F **(F)**. Intensity plots are drawn along the green lines of the cropped images.

Taken together, these data confirm that MTRIP probes are excluded from N- and P- containing inclusion bodies, but label cytoplasmic organelles that contain N, P, G and/or F proteins, as described previously [13]. These latter compartments are likely to have a different function than the RNA production activities of inclusion bodies and the data collected by ourselves and others [13] are consistent with them being an RSV-induced organelle, termed an assembly granule, that serves as a hub for collection of viral components prior to budding of RSV filamentous virions at the plasma membrane. The presence in these compartments of viral G-protein and N-RNA complexes that assemble through different pathways, argues against them being a cellular response to protein over-expression.

Cryo-Soft X-ray Tomography reveals the ultrastructure of assembly granules

The laser scanning confocal microscopy experiments described above confirmed the validity of G and MTRIP labelling for the identification and localisation of putative assembly granules, but G antibody labelling is not compatible with fixative-free cryogenic microscopy methods. Therefore, Alexa 488-conjugated lectin soyabean agglutinin (SBA) was used for fixative-free detection of G protein. SBA is a live-cell probe that specifically labels RSV G protein [13] (Fig S4D). A549 cells were propagated directly on gold electron microscopy grids, as described previously [18], infected with RSV and subsequently labelled with MTRIPs and SBA at 24 h pi to detect RSV genomic RNA and G protein. The grids bearing labelled, virus infected cells were then plunge frozen in liquid ethane. Frozen-hydrated grids were imaged at liquid nitrogen temperature by both epifluorescence and brightfield microscopy (Supplementary Fig S4, Fig 3A) to identify cells of interest exhibiting bright fluorescent labelling. Mock-infected cells were also stained, frozen and examined (Supplementary Fig S4). Having defined the regions of interest (ROI) by light microscopy, a montage of images that encompassed the whole grid was correlated with X-ray image montages of ROIs from the same

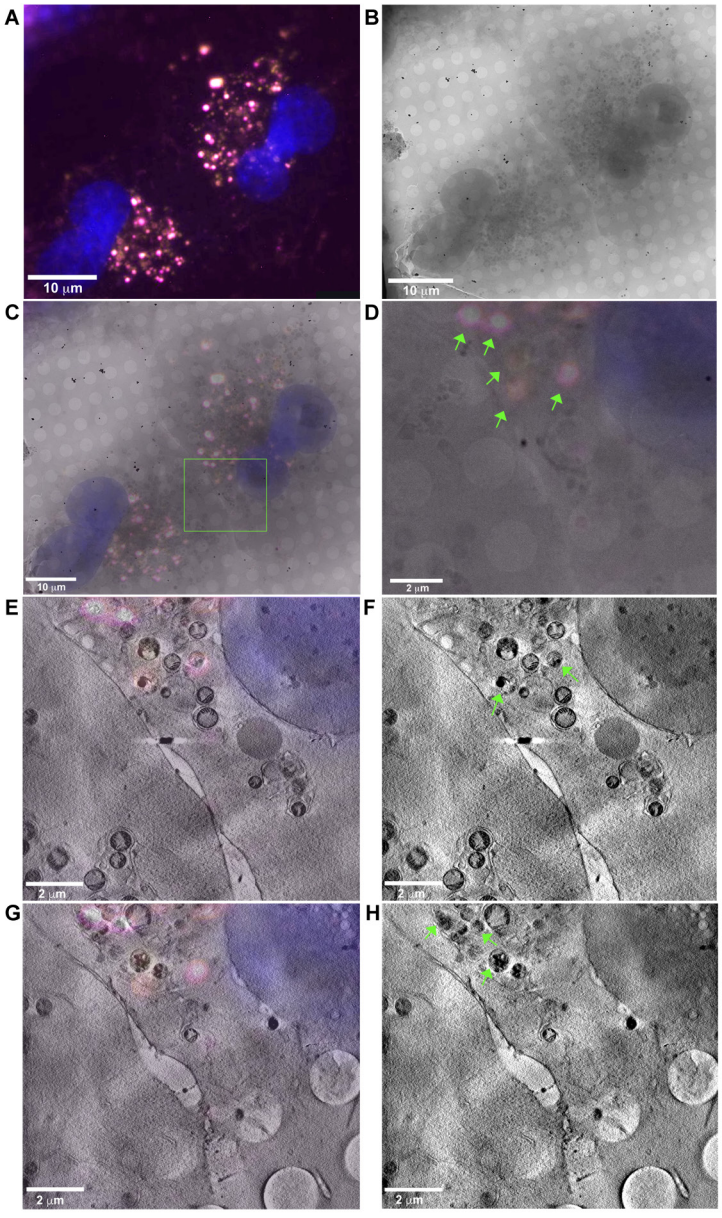

Figure 3. Correlated cryo fluorescence microscopy and cryo-SXT detects unique dense granular structures in frozen whole cells. A correlated imaging workflow combining cryo fluorescence and cryo-SXT was developed to image assembly granules and 3D ultrastructure of RSV infected cells. Guided by **(A)** cryo fluorescence, **(B)** X-ray image montages were collected from grid squares of interest. Fluorescence of G (yellow), viral RNA (pink) and the nucleus (blue) are shown. **(C)** Overlay of both light and X-ray microscopy images shows good correlation and ROIs (green square) were selected for image tilt-series collection. **(D)** Enlarged overlay image of the green square in (C) highlights several granular structures (green arrows) within the cytosol exhibiting strong fluorescence. **(E-H)** Tomographic slices show the presence of dense, high-contrast, granular structures (green arrows correspond to the same structures in D) correlating strongly with the bright fluorescence signals at higher resolution. Sequential slices of the same tomogram are depicted with (E and G) and (F and H) with and without the overlay for clarity.

samples using cryo-soft X-ray microscopy (Fig. 3B). Preliminary X-ray imaging allowed for assessment of ice quality and cell integrity as well as the presence of fiducial-markers, gold beads added to the specimen prior to freezing that enable accurate alignment of image tilt-series for three-dimensional (3D) reconstruction. Alignment and correlation of the X-ray and fluorescence microscopy image montages identified ROIs for tilt series data collection, targeting areas of the cytoplasm that showed RSV genome and G protein staining (Figs 3C and 3D). Overlaying slices from the resulting X-ray tomograms with the fluorescence microscopy data revealed that the fluorescent staining corresponded with the presence of cytoplasmic compartments (Figs 3E-3H).

Overall, 33 image tilt-series were collected for ROIs in RSV infected cells, while 17 image tilt-series were collected on representative cytoplasmic regions of mock-infected cells. The resulting tomograms revealed a cytoplasm full of membranous compartments in both infected and uninfected cells. Mitochondria were particularly evident and recognised by the presence of cristae. Lipid droplets were seen as dense bodies while

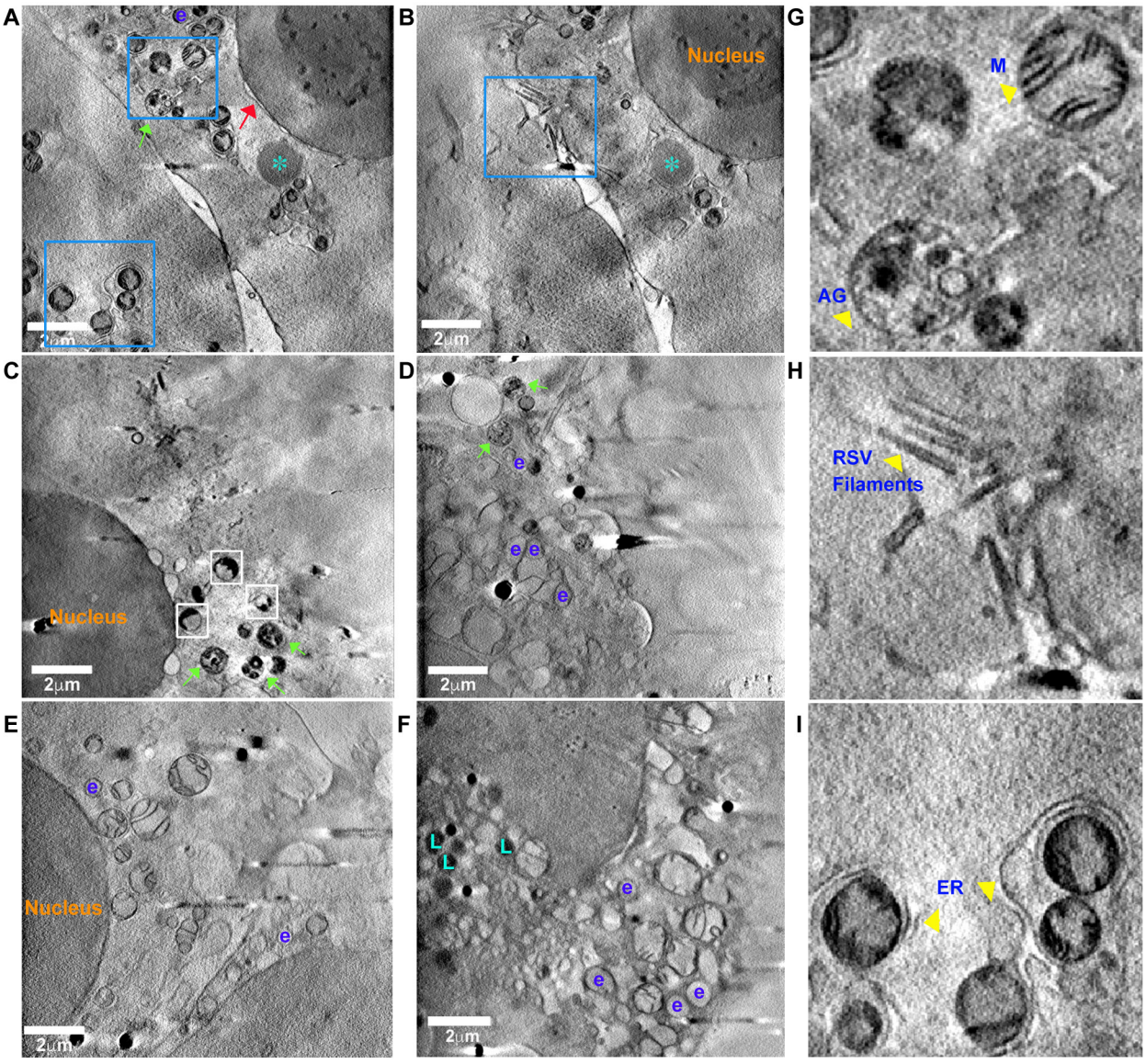

Figure 4. 3D architecture of RSV genome and G protein containing compartments revealed by correlative cryo-SXT. Soft X-ray tomography of RSV-infected and uninfected cells yielded a complex view revealing the extent of compartmentalisation in the cytoplasm. Various organelles are labelled - nucleus (orange), endosome 'e' (purple) and lipid droplets 'L' (cyan). **(A-D)** Unique membrane-bound multi-vesicular compartments (assembly granules) were visible in infected cells. **(A)** and **(B)** show two different slices through the same tomogram at different z-values. Assignment of compartments as assembly granules (green arrow) was made by correlation with fluorescent labelling of viral genome and RSV G. Other structures such as black-and-white dense compartments (white squares), putative inclusion bodies (cyan star) as well as blebbing of the nuclear membrane (red arrow) were also seen only in infected cells. **(E-F)** No assembly granule-like compartments were observed in mock-infected cells. Enlarged cropped images from (A) and (B) highlighted by blue squares, give a detailed view of **(G)** assembly granules (AG) and mitochondria (M); **(H)** RSV filaments and **(I)** the remodelling of the ER membrane. Relevant features are highlighted with yellow arrowheads.

an abundance of smaller compartments was also seen, presumably endosomes, lysosomes and similar. The cell nuclei, nucleoli and nuclear membranes were also readily observed (Fig. 4, supplementary videos 1 & 2). Guided by fluorescence microscopy data we identified membrane-bound, multi-vesicular compartments that correlated with the MTRIP and SBA staining, implicating them as assembly granules containing both viral RNA and G-protein (Figs 4A, 4C, 4D, 4G, supplementary video 1). Importantly these granular structures were evident only in RSV-infected samples and were not seen in mock-infected cells (Figs 4E, 4F, supplementary video 2). Assembly granules were observed to range in diameter from 435 nm to 762 nm and enclosed an abundance of smaller vesicles within them. They were often found to be closely apposed to mitochondria (Figs 4A, 4H), with both organelles often enwrapped in membrane (Figs 4A, 4I). These membranous changes seemed to originate from the periphery of the nucleus where we also observed blebbing of the nuclear membrane, suggesting that these membranes are derived from the endoplasmic reticulum (ER) (Fig. 4A).

RSV filamentous virions budding from the cell membrane were observed. These sites of virion assembly were occasionally found to be close to assembly granules (Fig. 4 A and B, G and H). As well as the fluorescently labelled multivesicular compartments, we saw several other structures in infected cells that were not seen in mock infected cells. These included large compartments that were denser than the cytosol but lacked a membrane, and that may be inclusion bodies (Figs 4A, 4B). We also saw many highly contrasted structures (Figs 4C, 4D, supplementary video 1). In the absence of specific labelling however we are unable to definitively ascribe a viral origin to these features.

These data provide a mesoscale view of the changes wrought upon cell architecture by RSV infection, showing an abundance of novel cellular compartments, consistent with the previous fluorescence imaging studies. With the aid of correlative microscopy, cryo-SXT shows that compartments labelled both for RSV genome and G protein are membranous, multi-vesicular organelles.

Assembly granules contain an abundance of uni- and multi-lamellar vesicles that enclose macromolecular assemblies likely composed of RSV nucleocapsid protein and RNA.

To achieve a higher resolution view of the assembly granules, we used correlative fluorescence microscopy to guide focused ion beam milling under cryogenic conditions (cryo-FIBSEM). This approach uses a specialised cryo-scanning electron microscope, fitted with an ion-beam source, to etch thin-sections from frozen-hydrated cells propagated directly on the cryo-EM grid. These ‘windows into the cell’ are known as lamellae [16]. Frozen-hydrated, RSV-infected A549 cells were imaged using epifluorescence microscopy to screen for MTRIP fluorescence and thereby determine ROIs likely to contain assembly granules for subsequent milling by cryo-FIBSEM. (Supplementary Fig. S5). Grids were imaged using the scanning-electron microscope probe at low (Fig. S5A) and medium magnifications (Figs S5B and S5C) allowing selection of cells that had previously shown good fluorescent labelling of puncta. The ROI was then milled using the gallium ion-beam to prepare a thin lamella (Fig. S5D-E). Grids bearing milled lamellae were carefully transferred to the cryo-TEM for tilt-series acquisition (Fig. S5F). The workflow for preparing lamellae is labour intensive and prone to build up of frost contamination and devitrification of the frozen materials. Despite the presence of some frosting, we were able to collect data on several lamellae that had remained wholly or mostly vitreous. In these preparations, cellular compartments were clearly visible in the cryo-EM at low magnifications (Fig. S5G and S5H). Dose-symmetric tilt series of selected ROIs were collected at a nominal magnification of 34,000×, corresponding to 3.48 Å/pixel at the specimen scale. These data were processed to calculate three-dimensional reconstructions (Fig. 5). Upon close inspection of the reconstructed tomograms, we see that each ROI contains a membrane bound compartment with complex ultrastructure comprising many smaller vesicles (Fig. 5, supplementary video 3).

The membranous organelle we see by cryo-ET has features consistent with those compartments seen at lower magnification by cryo-SXT (Figs 5A and 5B). Overall, the compartments range in diameter between 488 and 755 nm. Bound within the organelle are many tens of sub-compartments ranging in diameter between 35 nm and 240 nm. These vesicular sub-compartments are often flexible in shape deviating significantly from spherical form and sometimes folding around each other. Furthermore, these vesicles may be uni-lamellar, or multi-lamellar (Figs 5C, 5E). Many of the vesicles are densely packed with contents, especially the smaller ones, while others appear to have fewer contents. Vesicles occasionally appear to be connected

by junctions, with some having the appearance of being in a hemi-fusion state, suggesting dynamic mixing of contents (Figs 5D, 5F-5H). Within many larger sub-compartments, we noted the presence of ring-shaped and filamentous structures. We hypothesise that these macromolecular assemblies are likely N-RNA rings, loosely- and tightly-coiled helical nucleocapsids and/or holonucleocapsids (Figs 5I, 5J). The rings and helices ranged in diameter between 10 and 12 nm and are morphologically similar to holonucleocapsid and N-RNA rings seen previously in cryo-ET reconstructions of budding filamentous RSV virions [6]. Consistent with our cryo-SXT data, mitochondria were seen to be closely associated with these assembly granules (Figs 5A, B, C).

When viewing 3D tomographic reconstructions, sections through the reconstructed density maps do not readily convey the complexity of the volume information. To better visualize the 3D information present in these tomograms, we annotated an assembly granule by segmentation to produce a pseudo 3D representation of the organelle ultrastructure and surrounding cellular environment (Fig. 5K). The abundance of vesicular structures enclosed within the assembly granule, as well as the presence of N-RNA rings (Fig. 5J) is more easily appreciated in this representation, as is the proximity of a mitochondrion. ER-like membrane partially enwraps the assembly granule suggesting a possible role for ER-derived membrane in the formation of these compartments, a hypothesis supported by our cryo-SXT data (Fig. 5K).

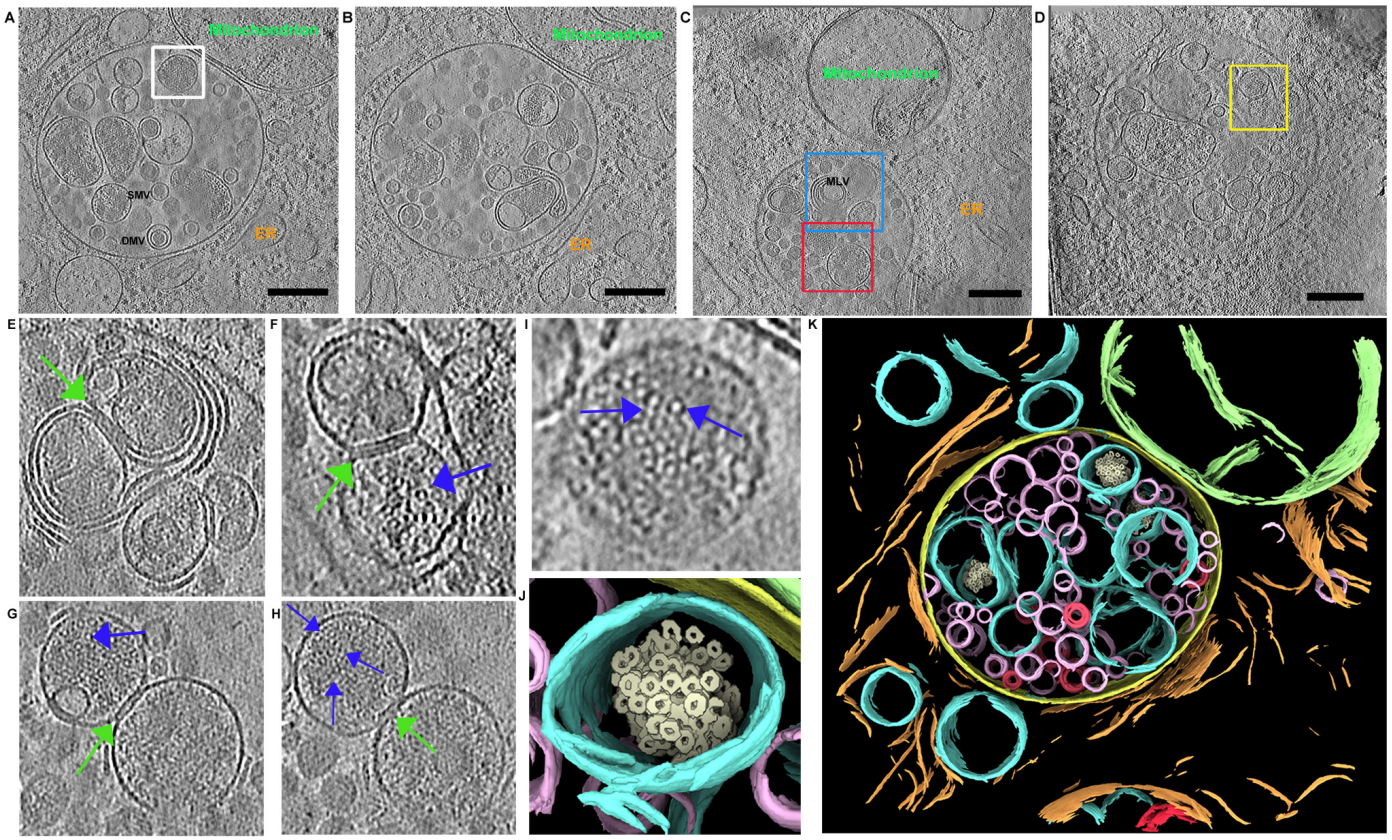

Figure 5. Assembly granules contain an abundance of vesicular sub-compartments. (A-B) Different z-slices of the same tomogram of an assembly granule and surrounding environment shows that the compartment is densely packed with differently sized vesicles and highlights a closely apposed mitochondrion and surrounding ER-like membranes, labelled in green and orange, respectively. Scalebar - 200 nm. **(C)** Many uni-lamellar and multi-lamellar vesicles are tightly packed within the organelle. **(D)** Vesicles within the organelle were sometimes seen to undergo fusion. Enlarged views of features indicated by **(E)** the blue square in (C) shows vesicles with multi-membranes while the **(F-H)** red and yellow squares in (C) and (D) show several vesicles that appear connected by junctions (green arrow). Some vesicles containing helical and ring structures (blue arrow) were found to be connected to other vesicles (green arrow) suggesting that they may be undergoing fusion and mixing of contents. **(G)** and **(H)** show different z-slices of the same tomogram. **(I)** Enlarged view of one such vesicle indicated by the white square in (A) shows ring and filamentous assemblies that we suggest are likely N-RNA and nucleocapsids (blue arrow). **(J)** Segmentation of this vesicle highlights the densely packed ring-like structures. **(K)** Segmentation showed the dense and complex environment of the assembly granule, revealing a membrane bound (yellow) compartment filled with differently sized vesicles, large (cyan) and small (pink) single membrane vesicles as well as double-membrane vesicles (red). Some vesicles contain putative nucleocapsids and N-RNA rings (cream). The organelle is seen closely apposed to a mitochondrion (green) and surrounded by ER membranes (orange).

Discussion

The formation of protein containing organelles in RSV infected cells has been documented in numerous studies. While the most frequently described are inclusion bodies, recent work has revealed that there are different types of structures with distinctive properties, as well as differences in associated proteins [10, 13, 19]. These findings are substantiated by the confocal microscopy analysis presented here, which revealed at least four types of distinctive structures: viral filaments at the plasma membrane, inclusion bodies, structures containing viral genome RNA, but not detected with other viral proteins, and assembly granules. In this study, we imaged RSV infected cells at a late time-point, when virions are assembling at the plasma membrane, to focus on assembly granules, structures that could be detected using live-cell probes and that contain viral genomic RNA and the G glycoprotein [13].

Assembly mechanisms differ across the non-segmented negative strand RNA viruses, even between closely related viruses, but in all cases examined to date, the process requires convergence of viral holonucleocapsids, matrix protein and surface glycoproteins [20, 21]. In the case of RSV, holonucleocapsids are generated in viral inclusion bodies [11]. Release of RSV holonucleocapsids from inclusion bodies is dependent on matrix protein, which transiently associates within inclusion bodies through interaction with the viral M2-1 protein [22-24]. The F protein also plays a role; it can be found localized within small puncta at the perimeter of inclusion bodies [25]. Transport of M and holonucleocapsids away from inclusion bodies and viral filament formation are dependent on the cytoplasmic C-terminal tail of F protein [26, 27] and microtubules, Rab11 and other components of the recycling endosome pathway [13, 19, 28, 29]. The G protein is trafficked to the plasma membrane independently of M and F [23, 30]. It is then internalized into vesicles in a clathrin-dependent manner and merges with granules containing viral holonucleocapsids and F protein [13]. It is these vesicles where the F- and M-associated holonucleocapsids and G proteins co-localise that are referred to as assembly granules [13].

The high-resolution multimodal analysis presented here shows for the first time the ultrastructural details of the assembly granules. Importantly, these tomogram images were captured by cryogenic vitrification of live RSV infected cells, preserving features that might have been lost or altered by fixation and staining. The data show that assembly granules are complex multi-vesicular structures. These are clearly distinct from the inclusion body RNA synthesis factories, which are membrane-less structures whose boundaries are defined by liquid-liquid phase separation [12, 31]. Each assembly granule consists of multiple, different types of vesicles collected within an organelle bounded by a single membrane. Some vesicles clearly contained viral nucleocapsids and N-rings, whereas others did not. There was evidence of channels and potential fusion events between these different vesicles. While we were not able to detect the glycoproteins or discern whether cellular or viral fusogens drive this process, such fusion events could allow vesicles containing RSV G protein to merge with vesicles harbouring F, M and viral holonucleocapsids, bringing the virion glycoproteins into the same membrane, with M and holonucleocapsids proximal to their cytoplasmic tails.

Unlike most other enveloped viruses RSV is not dependent on the ESCRT pathway for virus budding and fission [28]. This raises questions about how the budding process occurs. Live-cell and confocal microscopy studies of assembly granules showed that G- and F-containing vesicles distend into filaments which subsequently become loaded with genome RNA, indicating that assembly granules (and the vesicles within them) may play a role in virion formation [13]. However, another study showed that virions assemble at the plasma membrane [32]. Both findings are consistent with earlier EM studies that suggested that budding virions could be detected within intracellular vesicles as well as at the plasma membrane [33, 34]. It is possible that there is more than one pathway by which budding can occur. The images we collected do not show viruses budding within assembly granules, although considerably more images would need to be collected to rule out this possibility. However, we did observe close proximity of an assembly granule to budding virions at the plasma membrane (Fig. 4 A, B, G and H). It is possible that assembly granules function to transport the virion components to the plasma membrane and that vesicles within assembly granules then deposit their contents at the cytosolic side of the plasma membrane to begin the budding process. However, the complexity of these organelles makes it challenging to hypothesise mechanisms by which this may occur. Further high-resolution correlative cryo-EM studies may elucidate the processes leading to virion assembly.

In conclusion, to our knowledge this is the first study using state-of-the-art multimodal cryogenic correlative

imaging methods to carry out high-resolution ultrastructural characterisation of RSV assembly granules in live cells *in situ*. This work provides novel insights and opens new avenues for investigation concerning the enigmatic RSV assembly process.

Materials and Methods

Cells and virus

A549 cells were grown in Dulbecco's modified Eagle's medium (DMEM, Gibco, Life Technologies, UK) supplemented with 10% foetal bovine serum (FBS, Gibco, Life Technologies) at 37ºC and 5% CO2. When cells were about 75-80% confluent, virus infections were performed using the A2 RSV strain at a multiplicity of infection (MOI) of 3 in 2% DMEM for 6-, 12-, 18- and 24-h timepoints post infection (pi) to optimize the best time for imaging the live RNA probe.

Multiply-labelled Tetravalent RNA Imaging Probes (MTRIPs) assembly and delivery

Live cell fluorescent Alexa Fluor 594-conjugated MTRIPs targeting intergenic regions of the RSV genome were prepared as previously described [35]. Briefly, MTRIPs were activated and assembled by incubating them with neutravidin (Thermo Fisher Scientific) at a 5:1 molar ratio for 1 hour at room temperature. Probes were then filtered through a 30 KDa filter (Millipore Sigma) before use. MTRIPs were delivered into A549s via a reversible permeabilisation method with streptolysin O (Sigma). Infected cells were washed with PBS at 23 h (1 hour prior to the 24 h time point) and then incubated with a mixture of 0.2 U/ml of streptolysin O and the neutravidin-assembled probe in the appropriate amount of OPTIMEM for 10-12 min at 37 ºC. The streptolysin O, probe, OPTIMEM mixture was removed and replaced with fresh 2% DMEM at 37ºC for 30 minutes to allow cells to recover. Cells were then either fixed (4% formaldehyde) and permeabilised (0.2% Triton) for confocal fluorescence microscopy or labelled with the live SBA-G for fluorescence correlative microscopy.

Confocal light microscopy of fixed samples

A549 cells ($3x10^4$) were grown on 13 mm and 16 mm glass coverslips and infected as described above. Briefly A549 cells were infected with RSV strain A2 at an MOI of 3 for 1h and then washed with DMEM containing 2% FBS. After 23 h MTRIPs labelling was performed. Cells were then fixed and permeabilised one hour later - at 24 h pi with 4% formaldehyde and 0.2% Triton-X 100 in PBSA prior to staining with various antibodies specific to RSV proteins (F, G, N, P, M2-1). Fixed cells were blocked with sheep serum, donkey serum, or rabbit serum before staining with the primary antibody of interest for one hour at room temperature. Primary antibodies were mouse monoclonals obtained from Abcam, UK for the various viral proteins - B023 and RSV1C2 for N, RSV5A6 and RSV3216 for F, RSV133 for G, RSVH102 for P and RSV5H5 for M2-1. Following three PBS washes detection was carried out using goat, donkey or rabbit anti-mouse Alexa Fluor 488 secondary antibodies. Cells were mounted using Prolong Antifade plus DAPI reagent (Invitrogen, UK). Imaging was carried out using the Zeiss LSM880 laser scanning confocal microscope with a 63x/1.4NA oil immersion objective. Images were collected using GaAsP detector with 405 nm, 488 nm and 594 nm excitation lasers. Imaging processing and analysis was carried out with the Zeiss licenced software, Zeiss Zen Blue and Fiji [36].

Lectin soyabean agglutinin (SBA) RSV G protein labeling

SBA G was conjugated to Alexa Fluor 488 and generously provided by our collaborators at Georgia University of Technology. Post MTRIPs labeling (10-12 min), excess MTRIPs was washed away by adding fresh media, and cells allowed to recover for 30 min. A549 cells were then washed with PBS (without Ca^{2+} and Mg^{2+}), before being incubated with SBA G at a concentration of 20 ug/ml for 10 min. For co-localisation experiments with MTRIPs, cells were chilled on ice for 10 min and SBA-G labeling was carried out at 4ºC to minimize non-specific binding. Cells were then washed with PBS, replaced with fresh 2% DMEM, incubated at 37ºC for 10 min for cells to recover prior to imaging or plunge-freezing in ethane for cryo imaging experiments.

Cryo correlative light microscopy sample preparation

A549 cells were seeded directly on to cryo-EM grids prior to RSV infection as follows. Gold quantifoil R2/2 200 mesh grids (Quantifoil Micro Tools GmbH) were sterilised with 70% ethanol and placed in glass bottomed MatTek dishes (MatTek Corporation, USA). 200 ul of laminin (50 ug/ml) was added and incubated overnight at 37 ºC. Grids were then washed with 10% DMEM and seeded with $1x10^5$ cells at 37ºC, 5% CO_2 overnight. Cells were then infected with RSV-A2 at an MOI of 3 for 24 h. One hour prior to the desired time point of 24

h, MTRIPs and SBA-G labelling was performed sequentially, and cells left to recover for 30 min after labelling with MTRIPs and 10 min after SBA-G labelling at 37°C without fixation. Mock-infected cells were used as control. For X-ray imaging, 2-5 ml of concentrated 200 nm gold fiducials were added to the grids on the cell side before vitrification in liquid ethane using a Leica GP2 (Leica Biosystems, Germany). Fluorescence data on the vitrified grids was collected using a Linkam CMS196M cryo-correlative stage, fitted to a Zeiss Axio Imager 2 (Linkam Scientific Instruments, UK). Briefly, images were collected at 50× (0.55 NA) initially using bright-field (BF) or with filters 405 nm (blue channel), 488 nm (green channel) and 546 nm (red channel) to illuminate the fluorescent markers of interest and to obtain a general overview of the grid relating to its integrity, cell density and ice thickness. Tile imaging of the entire grid was then performed to generate a grid mosaic, following which specific ROIs were imaged at a higher magnification of 100×. Fluorescence images obtained were then used to guide cryogenic X-ray and EM imaging.

Cryo Soft X-ray Microscopy – data collection and analysis

Cryo-SXT was collected using the Zeiss UltraXRM-S220c cryo X-ray transmission microscope at beamline B24 (Diamond Light Source, Harwell, UK). Four samples were loaded onto the transfer shuttle at a time and then into the transmission X-ray microscope. Data were collected with X-rays at energy of 500 eV and focused with either 40 nm or 25 nm zone plates onto a direct detection CCD. For each grid, an initial bright field image of the entire grid was collected followed by X-ray montages of the squares of interest as identified by the correlative fluorescence data. Guided by the fluorescence data, ROIs within the squares were then selected for tilt series data collection at tilt angles -60º to +60º in 1º or 0.5º increments and an exposure of 0.5s or 1s per frame depending on area thickness. Tilt series were reconstructed using Etomo in IMOD [37] with an automated script available at B24. Alignment of fluorescence and X-ray data was carried out with Adobe Photoshop CS6 (Adobe, USA).

Cryo-FIBSEM milling of RSV-infected cells

RSV-infected A549 samples were prepared as described above with fluorescent MTRIPs, DAPI and G at an MOI of 3 for 24 h. Grids were then vitrified using the Leica GP2 with no gold fiducials added for cryo-FIBSEM milling. Cryo fluorescent imaging was carried out using the Linkam correlative stage as above before grids were clipped into autogrids, screened and milled at eBIC. Cryo-FIBSEM milling was carried out using a Scios DualBeam cryoFIB (ThermoFisher Scientific) equipped with a PP3010T transfer system and stage (Quorum Technologies) using the xT v7.6 software (ThermoFisher Scientific). Grids were sputter coated within the PP3010T transfer chamber (maintained at -175 °C). After loading onto the Scios stage (also maintained at -175 °C), the grids were inspected using the SEM (operated at 5 kV and 13 pA) and infected cells identified for milling based on previously recorded fluorescence data. The grid was coated with trimethyl(methylcyclopentadienyl)platinum(IV) (ThermoFisher Scientific) using the gas injection system incorporated into the SEM chamber to control milling rates and prevent curtaining artefacts at the leading edge. The thickness of this coating was ~3 µm. Milling was performed using a Ga^+ ion beam operated at 30 kV and currents decreasing from 300 to 30 pA, at an angle of 13° from the grid plane. At 30 pA the lamella thickness was typically <120 nm. During the final stage of milling, SEM inspection of the lamellae was conducted at 2 kV and 13 pA. Milled grids were stored in liquid nitrogen until further use.

Cryo-ET of lamellae – collection and processing

Cryo-FIB-milled lamellae were transferred to the 300 keV Titan Krios (Thermofisher, Netherlands) for imaging at eBIC (Harwell, UK). Milled lamellae were first identified at low magnification. Tilt series were then collected in a dose-symmetric tilt scheme at 300 kV and a magnification of 34,000× [38] using serialEM [39]. Data were collected over a tilt-range of -60º to +60º with a 3º increment, a total dose of 80 e/A^2 per tilt series, an applied defocus of -4 µm, pixel size of 3.479 Å and an energy filter with slit width of 20 eV. Frames were motion corrected using MotionCor2 [40], then dose weighted using Summovie [41] and aligned into angle ordered tilt series image stacks for further processing using IMOD. The Etomo package in IMOD was used to reconstruct the tomograms with frame alignment being performed by patch-tracking, as there were no gold fiducials [37]. CTF correction and defocus estimation was carried out using CTFFIND4 [42]. For visualization and interpretation, tomograms were binned by four and denoised with Topaz [43].

Segmentation/annotation

Segmentation was carried out using EMAN2 [44]. The assembly granule tomogram recorded from a cryo-FIB-

milled lamella was annotated using the convolutional neural network (CNN) based segmentation workflow menu of EMAN2. Briefly, each feature in the tomogram was trained individually using the CNN module. Robust training was performed by selecting 20-25 manually annotated image tiles (64x64 pixels) containing the feature of interest and 300-350 image tiles lacking the same feature. The trained CNN's were then applied to the tomogram and the output segmentations were visualised in ChimeraX [45].

Data Availability

LSM fluorescence images are deposited with the University of Glasgow Enlighten repository (DOI *). SXCT and cryo-ET data are deposited in EMPIAR (https://www.ebi.ac.uk/empiar/) (accession number ** and ** respectively). Representative cryo-ET tomograms are deposited in the EMDB (https://www.ebi.ac.uk/emdb/) (accession number **).

Acknowledgements

We acknowledge Diamond Light Source for time on Beamline B24 under Proposals MX14527, MX18331, MX19214, MX20556, and for access and support of the cryo-EM facilities at the UK's national Electron Bio-imaging Centre (eBIC) under proposal EM21016 (funded by the Wellcome Trust, MRC and BBRSC).
This work was supported by the United Kingdom Medical Research Council (MC_UU_12014/7 for DB, SV; MR/M000451/1 for DB, RF). RF, DB, PS, EB and AMB were supported by the United States of America National Institutes of Health (1R01AI113321).

The MRC-University of Glasgow Centre for Virus Research uses the CRediT taxonomy of author contributions. SV – investigation, methodology, validation, formal analysis, supervision, visualisation, writing – original draft; AMB – investigation, formal analysis, writing – review and editing; ELB – resources, writing - review and editing; MCS – investigation, writing – review and editing; JG – investigation, resources, writing – review and editing; AH – investigation, resources; MCD – investigation, writing – review and editing; MH – resources, writing – review and editing; CYW – methodology; RED – methodology, writing – review and editing; PS – resources, writing – review and editing; RF – conceptualisation, funding acquisition, writing – original draft; DB – conceptualisation, methodology, investigation, formal analysis, funding acquisition, supervision, visualisation, writing – original draft.

Conflict of Interest Statement

MCD is an employee of SPT Labtech Ltd. The remaining authors declare no relevant conflicts of interest.

References

1. Shi, T., et al., *Global, regional, and national disease burden estimates of acute lower respiratory infections due to respiratory syncytial virus in young children in 2015: a systematic review and modelling study.* Lancet, 2017. **390**(10098): p. 946-958.
2. Shi, T., et al., *Global Disease Burden Estimates of Respiratory Syncytial Virus–Associated Acute Respiratory Infection in Older Adults in 2015: A Systematic Review and Meta-Analysis.* The Journal of Infectious Diseases, 2019. **222**(Supplement_7): p. S577-S583.
3. Rima, B., et al., *ICTV Virus Taxonomy Profile: Pneumoviridae.* J Gen Virol, 2017. **98**(12): p. 2912-2913.
4. Collins, P.L., M.G. Hill, and P.R. Johnson, *The two open reading frames of the 22K mRNA of human respiratory syncytial virus: sequence comparison of antigenic subgroups A and B and expression in vitro.* J Gen Virol, 1990. **71 (Pt 12)**: p. 3015-20.
5. Collins, P.L., Y.T. Huang, and G.W. Wertz, *Identification of a tenth mRNA of respiratory syncytial virus and assignment of polypeptides to the 10 viral genes.* J Virol, 1984. **49**(2): p. 572-8.
6. Conley, M.J., et al., *Helical ordering of envelope-associated proteins and glycoproteins in respiratory syncytial virus.* EMBO J, 2022. **41**(3): p. e109728.
7. Walsh, E.E. and J. Hruska, *Monoclonal antibodies to respiratory syncytial virus proteins: identification of the fusion protein.* J Virol, 1983. **47**(1): p. 171-7.
8. Walsh, E.E., J.J. Schlesinger, and M.W. Brandriss, *Purification and Characterization of GP90, One of the Envelope Glycoproteins of Respiratory Syncytial Virus.* Journal of General Virology, 1984. **65**(4): p. 761-767.
9. Bachi, T. and C. Howe, *Morphogenesis and ultrastructure of respiratory syncytial virus.* J Virol, 1973. **12**(5): p. 1173-80.
10. Blanchard, E.L., et al., *Polymerase-tagged respiratory syncytial virus reveals a dynamic rearrangement of the ribonucleocapsid complex during infection.* PLoS Pathog, 2020. **16**(10): p. e1008987.
11. Rincheval, V., et al., *Functional organization of cytoplasmic inclusion bodies in cells infected by respiratory syncytial virus.* Nat Commun, 2017. **8**(1): p. 563.
12. Galloux, M., et al., *Minimal Elements Required for the Formation of Respiratory Syncytial Virus Cytoplasmic Inclusion Bodies In Vivo and In Vitro.* mBio, 2020. **11**(5).
13. Vanover, D., et al., *RSV glycoprotein and genomic RNA dynamics reveal filament assembly prior to the plasma membrane.* Nat Commun, 2017. **8**(1): p. 667.
14. Harkiolaki, M., et al., *Cryo-soft X-ray tomography: using soft X-rays to explore the ultrastructure of*

whole cells. Emerg Top Life Sci, 2018. **2**(1): p. 81-92.
15. Kounatidis, I., et al., *3D Correlative Cryo-Structured Illumination Fluorescence and Soft X-ray Microscopy Elucidates Reovirus Intracellular Release Pathway.* Cell, 2020. **182**(2): p. 515-530 e17.
16. Rigort, A., et al., *Micromachining tools and correlative approaches for cellular cryo-electron tomography.* J Struct Biol, 2010. **172**(2): p. 169-79.
17. Lifland, A.W., et al., *Human respiratory syncytial virus nucleoprotein and inclusion bodies antagonize the innate immune response mediated by MDA5 and MAVS.* J Virol, 2012. **86**(15): p. 8245-58.
18. Vijayakrishnan, S., et al., *Cryotomography of budding influenza A virus reveals filaments with diverse morphologies that mostly do not bear a genome at their distal end.* PLoS Pathog, 2013. **9**(6): p. e1003413.
19. Cosentino, G., et al., *Respiratory syncytial virus ribonucleoproteins hijack microtubule Rab11 dependent transport for intracellular trafficking.* PLoS Pathog, 2022. **18**(7): p. e1010619.
20. El Najjar, F., A.P. Schmitt, and R.E. Dutch, *Paramyxovirus glycoprotein incorporation, assembly and budding: a three way dance for infectious particle production.* Viruses, 2014. **6**(8): p. 3019-54.
21. Shaikh, F.Y. and J.E. Crowe, Jr., *Molecular mechanisms driving respiratory syncytial virus assembly.* Future Microbiol, 2013. **8**(1): p. 123-31.
22. Ghildyal, R., et al., *Respiratory syncytial virus matrix protein associates with nucleocapsids in infected cells.* J Gen Virol, 2002. **83**(Pt 4): p. 753-757.
23. Mitra, R., et al., *The human respiratory syncytial virus matrix protein is required for maturation of viral filaments.* J Virol, 2012. **86**(8): p. 4432-43.
24. Li, D., et al., *Association of respiratory syncytial virus M protein with viral nucleocapsids is mediated by the M2-1 protein.* J Virol, 2008. **82**(17): p. 8863-70.
25. Baviskar, P.S., et al., *The respiratory syncytial virus fusion protein targets to the perimeter of inclusion bodies and facilitates filament formation by a cytoplasmic tail-dependent mechanism.* J Virol, 2013. **87**(19): p. 10730-41.
26. Oomens, A.G., K.P. Bevis, and G.W. Wertz, *The cytoplasmic tail of the human respiratory syncytial virus F protein plays critical roles in cellular localization of the F protein and infectious progeny production.* J Virol, 2006. **80**(21): p. 10465-77.
27. Shaikh, F.Y., et al., *A critical phenylalanine residue in the respiratory syncytial virus fusion protein cytoplasmic tail mediates assembly of internal viral proteins into viral filaments and particles.* mBio, 2012. **3**(1).
28. Utley, T.J., et al., *Respiratory syncytial virus uses a Vps4-independent budding mechanism controlled by Rab11-FIP2.* Proc Natl Acad Sci U S A, 2008. **105**(29): p. 10209-14.
29. Brock, S.C., J.R. Goldenring, and J.E. Crowe, Jr., *Apical recycling systems regulate directional budding of respiratory syncytial virus from polarized epithelial cells.* Proc Natl Acad Sci U S A, 2003. **100**(25): p. 15143-8.
30. Jeffree, C.E., et al., *Ultrastructural analysis of the interaction between F-actin and respiratory syncytial virus during virus assembly.* Virology, 2007. **369**(2): p. 309-23.
31. Risso-Ballester, J., et al., *A condensate-hardening drug blocks RSV replication in vivo.* Nature, 2021. **595**(7868): p. 596-599.
32. Ke, Z., et al., *The Morphology and Assembly of Respiratory Syncytial Virus Revealed by Cryo-Electron Tomography.* Viruses, 2018. **10**(8).
33. Arslanagic, E., et al., *Maturation of respiratory syncytial virus within HEp-2 cell cytoplasm.* Acta Virol, 1996. **40**(4): p. 209-14.
34. Norrby, E., H. Marusyk, and C. Orvell, *Morphogenesis of respiratory syncytial virus in a green monkey kidney cell line (Vero).* J Virol, 1970. **6**(2): p. 237-42.
35. Santangelo, P.J., et al., *Single molecule-sensitive probes for imaging RNA in live cells.* Nat Methods, 2009. **6**(5): p. 347-9.
36. Schindelin, J., et al., *Fiji: an open-source platform for biological-image analysis.* Nat Methods, 2012. **9**(7): p. 676-82.
37. Kremer, J.R., D.N. Mastronarde, and J.R. McIntosh, *Computer visualization of three-dimensional image data using IMOD.* J Struct Biol, 1996. **116**(1): p. 71-6.
38. Hagen, W.J.H., W. Wan, and J.A.G. Briggs, *Implementation of a cryo-electron tomography tilt-scheme optimized for high resolution subtomogram averaging.* J Struct Biol, 2017. **197**(2): p. 191-198.
39. Mastronarde, D.N., *Automated electron microscope tomography using robust prediction of specimen*

movements. J Struct Biol, 2005. **152**(1): p. 36-51.

40. Zheng, S.Q., et al., *MotionCor2: anisotropic correction of beam-induced motion for improved cryo-electron microscopy.* Nat Methods, 2017. **14**(4): p. 331-332.
41. Grant, T. and N. Grigorieff, *Measuring the optimal exposure for single particle cryo-EM using a 2.6 A reconstruction of rotavirus VP6.* Elife, 2015. **4**: p. e06980.
42. Rohou, A. and N. Grigorieff, *CTFFIND4: Fast and accurate defocus estimation from electron micrographs.* J Struct Biol, 2015. **192**(2): p. 216-21.
43. Bepler, T., et al., *Positive-unlabeled convolutional neural networks for particle picking in cryo-electron micrographs.* Nat Methods, 2019. **16**(11): p. 1153-1160.
44. Chen, M., et al., *Convolutional neural networks for automated annotation of cellular cryo-electron tomograms.* Nat Methods, 2017. **14**(10): p. 983-985.
45. Pettersen, E.F., et al., *UCSF ChimeraX: Structure visualization for researchers, educators, and developers.* Protein Sci, 2021. **30**(1): p. 70-82.